The use of extended-defect dissolution as a probe for stress-induced interstitial diffusion anisotropy

P. Castrillo [a,*], R. Pinacho [a], M. Jaraiz [a], J.E. Rubio [a], J. Singer [b]

[a] Department of Electronics, University of Valladolid, ETSIT, Campus Miguel Delibes, 47011 Valladolid, Spain
[b] NXP Semiconductors, 850 rue Jean Monnet, 38926 Crolles, France

ARTICLE INFO

ABSTRACT

In this paper, the influence of biaxial strain-induced diffusion anisotropy on the evolution of extended defects in silicon has been analyzed. Point-defect diffusion anisotropy has been modeled and implemented within an atomistic kinetic Monte Carlo framework. The anneal of {3 1 1}-defects has been simulated for self-interstitial diffusion anisotropies varying within the plausible ranges. From these simulations, it is observed that diffusion anisotropy has a significant effect on the competition between defect ripening and dissolution. In particular, it is shown that the plot of {3 1 1} density versus {3 1 1} mean size could be used to check for the existence of self-interstitial diffusion anisotropy.

© 2008 Elsevier B.V. All rights reserved.

1. Introduction

Strained silicon is essential for the 45-nm node and beyond in order to improve device performance [1,2]. The strain could modify point-defect and dopant diffusion during device processing [3,4]. These modifications can be due to variations of the formation and migration energies of mobile species. Moreover, for biaxial strain, diffusion anisotropy may be induced due to inequivalence of in-plane and out-of-plane directions. At present, there is a controversy in theoretical studies about the magnitude (and even the existence) of diffusion anisotropy for point-defects and common dopants in the standard {1 0 0} orientation [5–7]. Available experimental information on diffusion anisotropy is indirect and only concerning dopants [8]. Besides, the available theoretical studies about the effect of strain on extended-defect dissolution do not consider the possible effect of anisotropic diffusion [9] and experimental data are not conclusive [10–12].

In this paper we analyze the effect of point-defect diffusion anisotropy on extended-defect dissolution. In particular, we focus on the case of {3 1 1}-oriented self-interstitial defects [13–15]. As a result, we propose {3 1 1}-defects as a probe of self-interstitial diffusion anisotropy.

* Corresponding author. Tel.: +34 645 689990; fax: +34 983423675.
E-mail address: Pedro.Castrillo@tel.uva.es (P. Castrillo).

2. Physical model

We consider biaxially strained {1 0 0} silicon layers, that can be obtained by epitaxial growth on a SiGe relaxed substrate [16]. Below the critical thickness for misfit dislocation nucleation, the in-plane lattice parameter of the epitaxy is imposed by the substrate ($a_{\text{in-plane}} = a_{\text{subs}}$). Thus, the biaxial strain of the silicon layer is $\varepsilon_{\text{biax}} = (a_{\text{subs}} - a_{\text{Si}})/a_{\text{subs}}$, where a_{Si} is the unstrained silicon lattice parameter. Knowing $\varepsilon_{\text{biax}}$, the stress σ_{biax} can be easily calculated according to $\sigma_{\text{biax}} = Y \cdot \varepsilon_{\text{biax}}$, where Y is the biaxial modulus.

Biaxial stress modifies the formation energy of intrinsic defects (self-interstitials, I, or vacancies, V) both when they are free point-defects and when they are bound to an extended defect. The binding energy (E_{b}) of an extended defect is given by the difference of the formation energy of the free and the bound I or V (i.e.: $E_{\text{b}}(\sigma_{\text{biax}}) = E_{\text{f}}^{\text{free}}(\sigma_{\text{biax}}) - E_{\text{f}}^{\text{bound}}(\sigma_{\text{biax}})$). For the case of {3 1 1}-defects, Guo et al. [9] calculated that E_{b} increases (decreases) for tensile (compressive) strain about 0.07 eV/%. This relatively small modification reflects that, for {3 1 1}-defects, $E_{\text{f}}^{\text{bound}}$ has a strain-dependence rather similar to $E_{\text{f}}^{\text{free}}$.

The transport capacity of point-defects is governed by the product of diffusivity and concentration (DC). This product is the relevant magnitude for diffusion processes and it is very difficult to split it experimentally into the individual contributions of D and C [17]. The activation energy of DC is $\Delta E_{\text{f}} + E_{\text{m}}$, where ΔE_{f} is the energy required to get a free point defect and E_{m} is its migration energy. In equilibrium conditions, ΔE_{f} is just the formation

energy of the point defect from surface ($\Delta E_f = E_f^{free}$). In contrast, during transient enhanced diffusion (TED) conditions, ΔE_f for self-interstitials is given by the binding energy required to get a free I from an extended {3 1 1}-defect ($\Delta E_f = E_b^{\{311\}}$) [13].

Under biaxial stress, the transport in the perpendicular direction, $DC_{33}(\sigma_{biax})$, is modified according to [8]:

$$\frac{DC_{33}(\sigma_{biax})}{DC(0)} = \exp\left(\frac{\sigma_{biax}V_{33}}{kT}\right) \tag{1a}$$

and in the in-plane direction, $DC_{11}(\sigma_{biax})$, is modified as:

$$\frac{DC_{11}(\sigma_{biax})}{DC(0)} = \exp\left(\frac{\sigma_{biax}V_{11}}{kT}\right), \tag{1b}$$

being $DC(0)$ the transport capacity for unstrained material, k the Boltzmann constant, T the temperature, and V_{33} and V_{11} the so-called apparent activation volumes in the perpendicular and in-plane directions, respectively. These activation volumes are the combination of the stress dependences of ΔE_f and of the migration energy in the corresponding direction (E_{m33} or E_{m11}):

$$V_{33} = \frac{-d(\Delta E_f + E_{m33})}{d\sigma_{biax}} \tag{2a}$$

$$V_{11} = \frac{-d(\Delta E_f + E_{m11})}{d\sigma_{biax}} \tag{2b}$$

As a consequence, under TED conditions, DC_{33} and DC_{11} would be affected in the same amount by the stress dependence of $E_b^{\{311\}}$.

If we focus the attention on the anisotropy, the ratio between the in-plane and perpendicular transport capacities can be written as:

$$\frac{DC_{11}}{DC_{33}} = \exp\left(\frac{A\varepsilon_{biax}Y\Omega}{kT}\right) \tag{3}$$

where Ω is one atomic volume and A is an adimensional anisotropy coefficient defined as $A = (V_{11} - V_{33})/\Omega$ [8]. As one can see in Eq. (3), the product $A\varepsilon_{biax}$ determines the diffusion anisotropy. If $A\varepsilon_{biax}$ is positive, in-plane diffusion is higher than the perpendicular one, being the opposite if $A\varepsilon_{biax}$ is negative. Moreover, one can notice from Eq. (2) that A does not involve ΔE_f and, therefore, would be the same in equilibrium and in TED conditions.

As far as we know, there are no experimental values of A for self-interstitials. A calculated value of +0.2 can be inferred from Ref. [7]. Anisotropy data for interstitial diffusers, that might be similar to that of Is, are very scattered. In the case of boron, experimental values of A for the standard {1 0 0}-orientation ranging from +1.2 to −1.1 have been inferred from the comparison of the perpendicular diffusivity under biaxial strain and the diffusivity under hydrostatic pressure [8,18,19]. In addition, the calculated values of A derived from ab-initio calculations are from 0 to +0.5 (with an upper limit of +0.8) for boron [5–8] and −1.4 for carbon [20]. To help elucidate this puzzle, we have found that the plot {3 1 1}-defect size versus {3 1 1}-defect density is selectively sensitive to the presence of I diffusion anisotropy. It might even provide a means for a quantitative estimate of the anisotropy coefficient A.

3. Model implementation

Our study has been carried out within the framework of atomistic non-lattice Kinetic Monte Carlo (KMC). The model described in the previous section has been included in the process simulator DADOS [21]. Ion-implant generated Is and Vs are calculated within the Binary Collision Approximation and loaded into DADOS. This simulation scheme has been proven to reproduce very well the phenomenology of extended-defect evolution for the relaxed

material [15,21]. A description of our extended-defect implementation, focused on {3 1 1}-defects, is given in Ref. [15]. In particular, we assume that the length of a {3 1 1}-defect ($L_{\{311\}}$) depends on the number of Is (n_I) as $L_{\{311\}} \approx 0.43\,n_I^{2/3}$ nm.

In our simulations, the surface is assumed to be a perfect sink for Is (i.e. the recombination occurs with no barrier) [22] whereas lateral and bottom boundaries are assumed to act as perfect mirrors (i.e. the jump is rejected) [23]. This assumption for the bottom boundary is valid for the realistic cases of both silicon on silicon (with low trap density and back surface far away) and silicon on SiGe (assuming that DC_{33} for Is in the SiGe substrate is lower than in a tensile Si layer grown on it). No misfit dislocations are assumed.

Concerning the splitting of the strain dependence of the DC product, we assume that strain modifies ΔE_f whereas the migration rate is unaffected. Strain-induced diffusion anisotropy is implemented assigning different jump probability for Is in the in-plane and perpendicular directions, according to Eq. (3). Following Ref. [9], the strain dependence of binding energies of {3 1 1}-defects has been assumed to be independent of size, with a value of 0.07 eV/% [9].

4. Simulation results

As a representative case, we have simulated a 5×10^{13} cm^{-2} 40 keV Si$^+$ implant followed by an 815 °C anneal. This process is non-amorphizing, does not involve dopants, and gives rise to {3 1 1}-defects detectable by Transmission Electron Microscopy (TEM) [13,14]. We have used a simulation cell with an implant-area of 200 nm × 200 nm and a depth of 500 nm that is large enough to contain the whole implant cascade damage, which is within a depth of 400 nm. We have verified that larger depths do not lead to relevant differences in the simulation results.

First, following Ref. [9], we have performed simulations assuming no anisotropy ($A = 0$) for both tensile (+1%) and compressed (−1%) material, and we have compared them to the unstrained one [24]. In Fig. 1(a) and (b), we have represented the anneal time evolution of {3 1 1}-defect areal density ($d_{\{311\}}$) and mean length ($\langle L_{\{311\}} \rangle$), respectively. Only {3 1 1}-defects longer than 5 nm ($n_I > 40$) are taken into account in order to emulate the TEM threshold sensitivity. As it can be seen in the figure, and in agreement with Ref. [9], tensile stress retards and compressive stress accelerates defect evolution. This is due to the strain-induced modification of E_b and, consequently, of I-emission rate of {3 1 1}'s. In Fig. 1(c), $\langle L_{\{311\}} \rangle$ has been plotted versus $d_{\{311\}}$ and the time variable has been omitted. As a reference, lines corresponding to different values of the total self-interstitial areal density (ρ_I) are indicated in the figure. As it is apparent in Fig. 1(c), the three cases follow the same evolution path, although with a different time scale.

Fig. 1(c) is useful to visualize the three stages of {3 1 1} evolution during the annealing: (1) *Nucleation stage*: Is and Vs recombine and excess Is are trapped by clusters. As a result many small {3 1 1}-defects start to grow, entering into the TEM-detectable size range. This is reflected in the figure, where $d_{\{311\}}$ and ρ_I increase and $\langle L_{\{311\}} \rangle$ is maintained near the minimum detectable size. The maximum of ρ_I (~2.5×10^{13} cm^{-2}) is only half of the +1 model prediction because Is in small clusters are not taken into account. (2) *Ripening stage*: After nucleation, defect dynamics is driven by the emission of Is from {3 1 1}'s. Emitted Is can be trapped by other {3 1 1}'s or (to a lower extent) are annihilated at the surface. As a consequence, large {3 1 1}'s (more stable) grow, small {3 1 1}'s disappear, and the total amount of Is scarcely decreases (quasi-conservative ripening) [13–15]. Thus, $\langle L_{\{311\}} \rangle$ increases, $d_{\{311\}}$ decreases, and ρ_I slightly diminishes. (3) *Dissolution stage*: When the mean distance between {3 1 1}'s becomes larger than the distance to the surface,
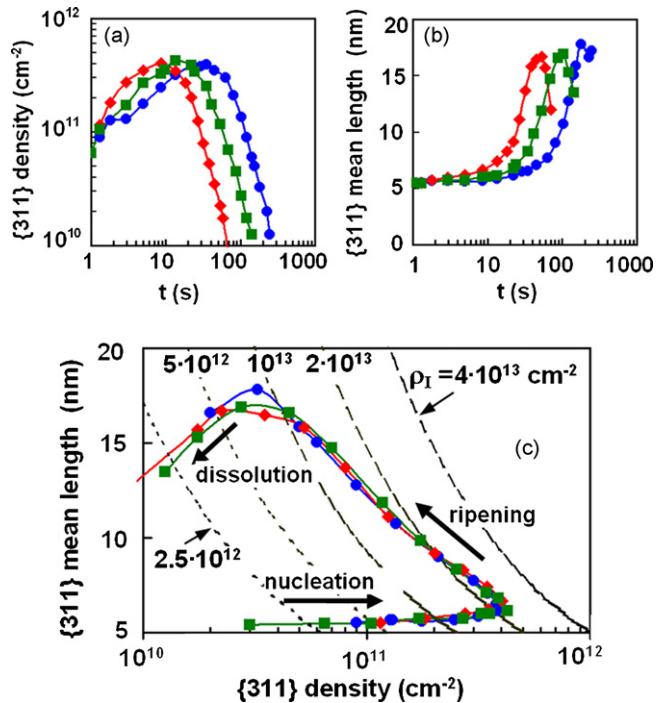
Fig. 1. Simulated evolution of {3 1 1}-defects in silicon for a 5×10^{13} cm^{-2}, 40 keV, Si$^+$ implant followed by an 815 °C anneal, for a tensile biaxial strain of $\varepsilon_{biax} = +1\%$ (circles), a compressive biaxial strain of $\varepsilon_{biax} = -1\%$ (diamonds), and unstrained material (squares), assuming no diffusion anisotropy. (a) Anneal time evolution of {3 1 1}-defect density. (b) Anneal time evolution of {3 1 1}-defect mean length. (c) {3 1 1} Mean length versus {3 1 1} density plot built from (a) and (b). Dashed lines correspond to constant values of the total density of self-interstitials in {3 1 1}-defects, ρ_I. Nucleation, ripening, and final dissolution stages are indicated in the figure.

most of the emitted Is recombine at the surface [15]. Then, {3 1 1}'s dissolve and $\langle L_{\{311\}} \rangle$, $d_{\{311\}}$, and ρ_I decrease. It is worthy to point out that when the number of {3 1 1}-defects in the simulation domain becomes small the statistic noise in the simulation becomes large. Therefore, data of the dissolution stage, that in Fig. 1(c) are below $d_{\{311\}} = 3 \times 10^{10}$ cm^{-2} corresponding to less than 12 defects, are highly affected by statistical uncertainties.

The evolution path on the $\langle L_{\{311\}} \rangle$ versus $d_{\{311\}}$ diagram depends on the competition between ripening and dissolution. The strain-induced dependence that we have considered in Fig. 1 does not modify the path because both ripening and dissolution are accelerated or retarded to the same extent. Besides, if the anneal temperature of the simulation is changed (going for example to 670 (C) the evolution time-scale varies several orders of magnitude but the trajectory of $\langle L_{\{311\}} \rangle$ versus $d_{\{311\}}$ only shows minor changes with respect to Fig. 1(c) and the compressive and tensile simulations follow again the same path that the unstrained one.

It is interesting to realize that, during the ripening stage, {3 1 1}-defects are located in a buried layer parallel to the surface [13,14]. As a result, their dissolution is related to I-transport in the perpendicular direction (DC_{33}) whereas their ripening is mainly due to in-plane I-transport (DC_{11}). Therefore, a strain-induced anisotropy of self-interstitial diffusion would modify the competition between ripening and dissolution and is expected to affect the path on the $\langle L_{\{311\}} \rangle$ versus $d_{\{311\}}$ graph. In order to test this idea, we have simulated the process of Fig. 1 with different diffusion anisotropies and we have represented them in Fig. 2. The values of $A\varepsilon_{biax}$ that we have used are +0.3% and −0.3%, that correspond to DC_{11}/DC_{33} ratios of about 2 and 0.5, respectively. In particular, we have assumed $A = \pm 0.6$ and $\varepsilon_{biax} = 0.5\%$. This ε_{biax} would correspond to a pseudomorphic silicon layer grown on a relaxed Si$_{0.88}$Ge$_{0.12}$

pseudo-substrate [25] while A values are within the experimental range for the anisotropy of Boron [8]. Simulated results for $\varepsilon_{biax} = 0$ are also represented for comparison. As it was expected, the differences in the evolution path caused by diffusion anisotropy are evident in Fig. 2, in clear contrast with the isotropic case of Fig. 1(c) and the effect of the anisotropy is especially noticeable during the ripening stage. Thus, for $A\varepsilon_{biax} > 0$ (i.e.: $DC_{11} > DC_{33}$) defect growth is favored respect to dissolution. In consequence, the evolution path has an almost constant ρ_I and the values reached by $\langle L_{\{311\}} \rangle$ are large. The opposite behavior is observed for $A\varepsilon_{biax} < 0$. Fig. 3 displays the atomistic snapshots and the defect size histograms corresponding to the three points marked in Fig. 2, all of them for the same defect density. As it is illustrated there, the diffusion anisotropy affects not only the mean defect size but also to the defect size distribution.

Some modifications of the values of ρ_I are observed at the end of the nucleation stage in Fig. 2 ($\rho_I = 2 \times 10^{13}$ for $A\varepsilon_{biax} = -0.3\%$, 2.5×10^{13} for $A\varepsilon_{biax} = 0$, and 3.1×10^{13} for $A\varepsilon_{biax} = 0.3\%$). In principle, one could expect that these changes would be translated into non-negligible modifications of the "+N" factor for dopant diffusion [13]. However, we have verified that, at the end of the simulations, the total number of I hops in the perpendicular direction is virtually the same for the three cases of Fig. 2, although the evolution times are quite different. This means that although the +N number measurable by microscopy is expected to be different, the effective +N for dopant diffusion will be the same. The discrepancies of ρ_I values are due both to Is that have recombined at the surface during the nucleation stage and to Is in small undetectable clusters.

It is necessary to be aware of other contributions, besides diffusion anisotropy, which could also modify the defect evolution path. In particular, the ripening of {3 1 1}-defects might be affected if (contrary to the assumption of Ref. [9]) $\partial E_b / \partial \varepsilon_{biax}$ depends on n_I or if the geometry of {3 1 1}-defects depends not only on n_I but also on the strain. As far as we know, there are neither experimental evidence nor reliable calculations about these dependences and, in consequence, we have not included them in our simulations. Nevertheless, we have verified that the diffusion anisotropy effects are also present for {3 1 1}-defect geometries different from the one described in the previous section. In particular, if a constant width is assumed (for example, 5 rows width and $L_{\{311\}} = 0.06 n_I$) the con-
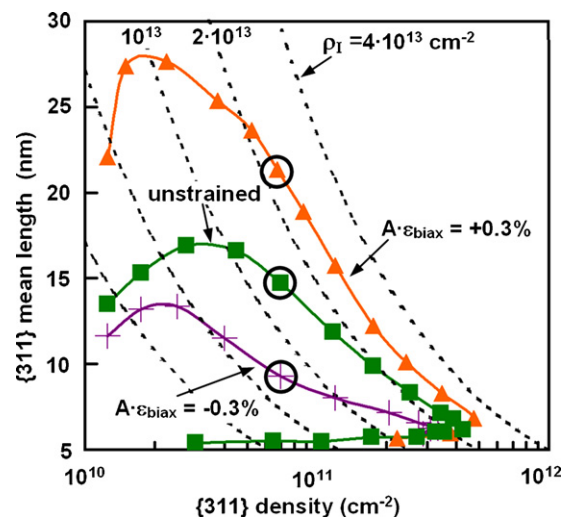

Fig. 2. Simulated {3 1 1}-defect mean length versus {3 1 1}-defect density for the process of Fig. 1, but anisotropic diffusion with $A\varepsilon_{biax} = +0.3\%$ (triangles) and $A\varepsilon_{biax} = -0.3\%$ (crosses). The unstrained case is also shown as a reference (squares). Dashed lines correspond to constant values of ρ_I. Open circles indicate the evolution points used for Fig. 3.
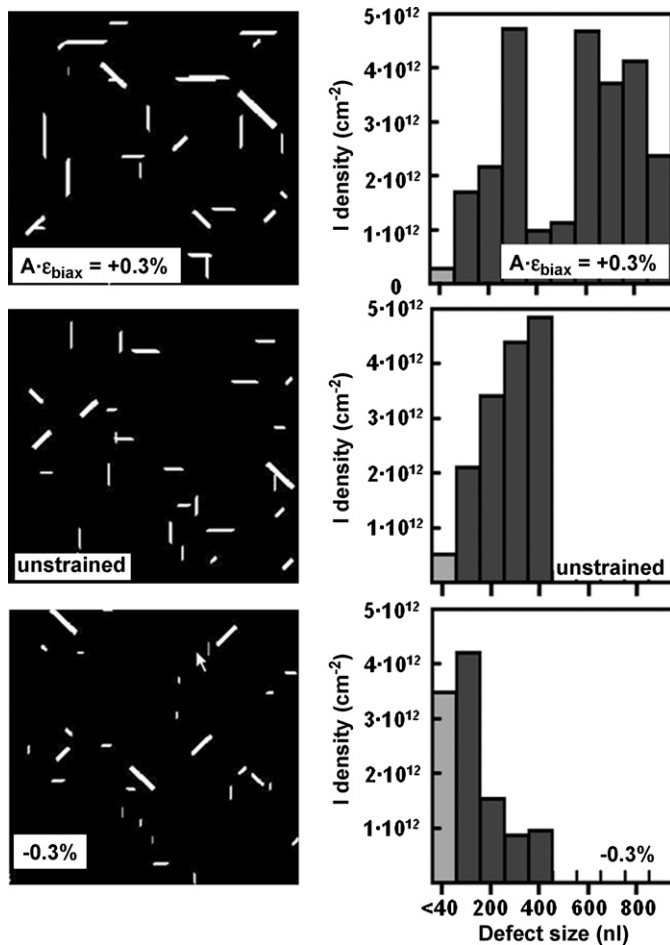
Fig. 3. Atomistic snapshots (left) and defect size histograms (right) for the three evolution points marked in Fig. 2. They correspond to a same {3 1 1}-defect density of 7×10 cm^{-3} but to different values of $A\varepsilon_{biax}$: +0.3% (top), 0% (middle), and −0.3% (bottom). Snapshots are 200 nm × 200 nm plan views and only defects larger than 40 Is are visualized. Histograms represent the number of Is per unit area, sorted by defect sizes (expressed in number of Is). The contribution of Is in defects smaller than 40 Is is represented in lighter gray.

sequences of anisotropy are even more dramatic than those shown in Figs. 2 and 3.

5. Conclusions

In summary, we have studied the influence of strain-induced self-interstitial diffusion anisotropy on the dissolution of {3 1 1}-defects. Diffusion anisotropy has been assessed through the apparent activation volumes V_{33} and V_{11}, with a treatment valid for both equilibrium and TED conditions. We have verified that isotropic modifications (for example, of E_b or anneal temperature), which can change the time scale by even orders of magnitude, hardly modify the evolution path on the $\langle L_{\{311\}} \rangle$ versus $d_{\{311\}}$ diagram. In contrast, modifications of a factor 2 of the DC_{11}/DC_{33} ratio cause remarkable changes in the evolution path. The effect of diffusion anisotropy is mainly a change in the competition between defect ripening, favored by in-plane transport, and defect dissolution, favored by perpendicular transport. The analysis of the $\langle L_{\{311\}} \rangle$ versus $d_{\{311\}}$ evolution path could provide a way to experimentally assess the anisotropy coefficient. Diffusion anisotropy could also modify the defect size distribution and, as a consequence, the number of Is detectable by TEM, but it would not alter the effective +N number for dopant diffusion.

References

[1] K. Mistry, et al., International Electron Device Meeting, IEEE, Piscataway, 2007, p. 247.
[2] L. Peters, Semiconduct. Int. 30 (2007) 40.
[3] N.E.B. Cowern, P.C. Zalm, P. van der Sluis, D.J. Gravesteijn, W.B. de-Boer, Phys. Rev. Lett. 72 (1994) 2585.
[4] A. Nylandsted-Larsen, N. Zangenberg, J. Fage-Pedersen, Mater. Sci. Eng. B 124–125 (2005) 241.
[5] M.S. Daw, W. Windl, N.N. Carlson, M. Laudon, M.P. Masquelier, Phys. Rev. B 64 (2001) 045205.
[6] L. Lin, T. Kirichenko, B.R. Sahu, G.S. Hwang, S.K. Banerjee, Phys. Rev. B 72 (2005) 205206.
[7] M. Diebel, S.T. Dunham, International Conference on Simulation of Semiconductor Processes and Devices, IEEE, New York, 2003, p. 147.
[8] M.J. Aziz, Y. Zhao, H.J. Gossmann, S. Mitha, S.P. Smith, D. Schiferl, Phys. Rev. B 73 (2006) 054101.
[9] H.W. Guo, S.T. Dunham, C. Shih, C. Ahn, International Conference on Simulation of Semiconductor Processes and Devices, IEEE, Piscataway, 2006, p. 71.
[10] S. Chaudhry, M.E. Law, J. Appl. Phys. 82 (1997) 1138.
[11] P.F. Fazzini, F. Cristiano, C. Dupré, A. Claverie, T. Ernst, M. Gavelle, J. Vac. Sci. Technol. B 26 (2008) 342.
[12] V. Moroz, I. Martin-Bragado, S. Felch, F. Nouri, C. Olsen, K.S. Jones, J. Vac. Sci. Technol. B 26 (2008) 439.
[13] P.A. Stolk, H.-J. Gossmann, D.J. Eaglesham, D.C. Jacobson, C.S. Rafferty, G.H. Gilmer, M. Jaraiz, J.M. Poate, H.S. Luftman, T.E. Haynes, J. Appl. Phys. 81 (1997) 6131.
[14] F. Cristiano, N. Cherkashin, X. Hebras, P. Calvo, Y. Lamrani, E. Scheid, B. de Mauduit, B. Colombeau, W. Lerch, S. Paul, A. Claverie, Nucl. Instr. Meth. B 216 (2004) 46.
[15] I. Martin-Bragado, I. Avci, N. Zographos, M. Jaraiz, P. Castrillo, Solid State Electron. 52 (2008) 1430.
[16] R. People, J. Quantum Electron 22 (1986) 1696.
[17] H.J. Gossmann, J.M. Poate, in: M. Scheffler, R. Zimmermann (Eds.), Proceedings of 23rd International Conference on the Physics of Semiconductors, vol. 4, World Scientific, Singapore, 1996, p. 2569.
[18] P. Kuo, J.L. Hoyt, J.F. Gibbons, J.E. Turner, D. Lefforge, Appl. Phys. Lett. 66 (1995) 580.
[19] N.R. Zangenberg, J. Fage-Pedersen, J. Lundsgaard-Hansen, A. Nylandsted-Larsen, J. Appl. Phys. 94 (2003) 3883.
[20] H.W. Guo, C. Ahn, S.T. Dunham, Mat. Res. Soc. Sym. Proc. 1070 (2008), E03–07.
[21] M. Jaraiz, P. Castrillo, R. Pinacho, J.E. Rubio, International Electron Device Meeting, IEEE, Piscataway, 2007, p. 951.
[22] N.E.B. Cowern, D. Alquier, M. Omri, A. Claverie, A. Nejim, Nucl. Instr. Meth. B 148 (1999) 257.
[23] M. Jaraiz, L. Pelaz, E. Rubio, J. Barbolla, D.J. Eaglesham, H.J. Gossmann, J.M. Poate, Mater. Res. Soc. Symp. Proc. 532 (1998) 53.
[24] For ε_{biax} = 1%, the critical thickness for the nucleation of misfit dislocations in silicon is only 100 nm (see Ref.16). In contrast, the depth affected by the damage of a 40 KeV Si$^+$ implant is about 400 nm. This suggests that the strain values used in Ref.9 (and employed in Fig. 1) are unrealistically high and valid only to rule out the relevance of the strain-dependence of the Eb of {3 1 1}-defects.
[25] For ε_{biax} = 0.5% the critical thickness of silicon is about 700 nm [16]. Therefore, it could be feasible to grow a dislocation-free, 0.5% strained, silicon layer with a thickness of 400 nm, which would be suitable for the process of Fig. 3.